

A Fast Electron Transport Model for Lower Hybrid Wave Sustained Plasmas

Akira EJIRI, Hibiki YAMAZAKI, Yuichi TAKASE^{a)}, Naoto TSUJII, Osamu WATANABE, Yi PENG, Kotaro IWASAKI, Yuki AOI, Yongtae KO, Kyohei MATSUZAKI, James H.P. RICE, Yuki OSAWA, Charles P. MOELLER¹⁾, Yasuo YOSHIMURA²⁾, Hiroshi KASAHARA²⁾, Kenji SAITO²⁾, Tetsuo SEKI²⁾ and Shuji KAMIO²⁾

The University of Tokyo, Kashiwa 277-8561, Japan

¹⁾*General Atomics, San Diego, CA 92186, U.S.A.*

²⁾*National Institute for Fusion Science, Toki 509-5292, Japan*

(Received 20 October 2021 / Accepted 10 March 2022)

In the TST-2 spherical tokamak (ST), non-inductive start-up by lower-hybrid waves (200 MHz) has been studied and a plasma current of 27 kA was achieved. For a comprehensive understanding of the wave sustained plasmas, a fast electron transport model combined with an X-ray emission model is constructed. The electrons in the model show a velocity random walk induced by the wave and collisional slowing down. Simultaneously, they show diffusion in real space. Electron generation and loss at the limiters are also considered. Using the model we can calculate the powers, such as the power from the wave to electrons (i.e., deposition power), collisional bulk electron heating power, power to the limiters. In addition, plasma current, electron density, neutral density, X-ray spectrum expected by a certain measurement system are obtained. Comparison with experimental data shows that a major part of the LHW deposition power is lost by fast electrons hitting the outboard limiter, while a minor part is used to heat cold bulk electrons. The diffusion in real space is well described by the RF induced radial transport, which is often used to interpret fast ion diffusion in ICRF heating. The present work suggests that the RF induced transport of fast electrons is the dominant loss mechanism.

© 2022 The Japan Society of Plasma Science and Nuclear Fusion Research

Keywords: rf induced transport, lower hybrid wave, spherical tokamak, fast electron

DOI: 10.1585/pfr.17.1402037

1. Introduction

Noninductive plasma current start-up and sustainment is a critical issue in fusion research, particularly in spherical tokamak (ST) devices, in which there is almost no space for the central solenoid. RF current drive is one of standard current drive methods, and electron cyclotron waves are used in many ST devices. On the other hand, in TST-2 spherical tokamak [1], we use lower hybrid wave (LHW), which is known to be efficient in conventional tokamaks. Experiments using various antennas were performed [2–6], and a plasma current of 27 kA was generated and sustained [7]. Although the current is about one fourth of standard inductive discharges in TST-2, the current drive efficiency is not sufficient so far, and further improvement is required. According to a wave simulation, the wave power is deposited mainly at the peripheral region, and orbit loss is significant [8].

Hard X-rays are emitted from confined fast electrons through bremsstrahlung and the energy and profile of hard X-ray emission are believed to reflect the properties of fast

electrons. In TST-2, however, the measured hard X-ray and soft X-ray emissions during RF power modulation shows rapid increase or decrease at RF power on and off, while the plasma current shows little variation during the modulation [9]. In addition, the soft X-ray measurement by two detectors with different thin foils in front of them suggests characteristic X-ray emission of iron. These results indicate that a significant fraction of the measured hard X-ray emission is thick target X-ray, which is generated at a limiter when a fast electron hits it. In order to interpret the behaviours of the X-ray emission, we propose an RF induced transport model combined with an X-ray emission model. When the RF induced transport is the dominant loss mechanism of fast electrons, the loss would abruptly disappear at the RF turn off, and the experimental rapid decrease (within about 10 μ s [9]) in the hard X-ray emission would be explained by the model. Note that the RF induced transport effect cannot be explicitly considered in the conventional tool: GENRAY and CQL3D, which we have used [8]. The objectives of the present study are the qualitative reproduction of the experimental features and the prediction of the order of the measured quantities which are believed to be related to fast electrons.

author's e-mail: ejiri@k.u-tokyo.ac.jp

^{a)} Present affiliation: Tokamak Energy Ltd., Milton Park OX14 4SD, United Kingdom

The paper is organized as follows. An RF induced transport model is described in Sec. 2. A hard X-ray emission model is described in Sec. 3. Comparisons between measured and predicted X-ray spectra are given in Sec. 4. Some other predicted quantities are also presented and discussed. Section 5 provides discussion. The conclusions are given in Sec. 6.

2. RF Induced Transport Model

Figure 1 shows the schematic configuration of the electron transport model. A cold electron starting from a magnetic surface is accelerated along a magnetic field line by the LHW electric field. With the increase in the parallel velocity the orbit deviates from the magnetic surface, and the electron would hit the outboard limiter or the inboard limiter. Besides the LHW electric field, collisions with ions, electrons and neutrals would decrease the speed of electron, by which the orbit moves inward. The effect of the LHW electric field is simulated by a random walk in velocity space, which also induces a spatial random walk. The electron reaching a limiter is lost, and a new cold electron is supplied on a given magnetic surface to keep a steady state. By following many electrons we would obtain a velocity distribution function. From the analysis of the obtained state, power from LHW to fast electrons, collisional heating power of cold electrons, the current carried by fast electrons, particle confinement time can be calculated. In the following, the detail of the model is described.

An electron starts from a magnetic surface, of which inboard and outboard major radii at the midplane are R_{sin}

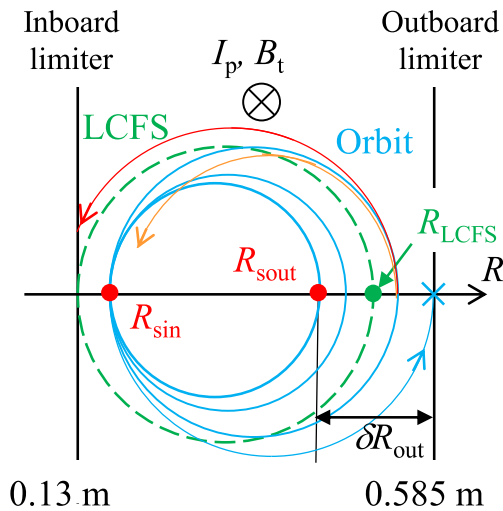


Fig. 1 Schematic configuration in a poloidal plane. The solid light blue curve shows the orbit of an electron accelerated at the position R_{sin} . The corresponding outboard starting point position is R_{sout} , and the distance between R_{sout} and the outboard limiter (at $R = 0.585$ m) is defined as δR_{out} . The outboard last closed flux surface (LCFS) position is R_{LCFS} . The red and orange orbits show the cases of the outboard deceleration and acceleration, respectively.

and R_{sout} , respectively. The electron is accelerated or decelerated by the electric field of the LHW. Here, we assume that the acceleration or deceleration occurs only at the midplane. The canonical angular momentum of the electron is conserved between the accelerations or decelerations at the midplane: $-eRA_\phi + m_eRV_\phi = const$. Here, V_ϕ is the toroidal components of the velocity and $V_\phi < 0$ for the plasma current carrying electrons, and $RA_\phi (> 0)$ is the poloidal flux. The canonical momentum at the inboard midplane point R_{in} and that at the outboard midplane point R_{out} is the same when no acceleration or deceleration occurs, and it is written as

$$-eRA_\phi|_{R_{in}} + m_eR_{in}V_{||} = -eRA_\phi|_{R_{out}} + m_eR_{out}V_{||}. \quad (1)$$

Here, $V_{||}$ is the parallel velocity. R_{in} and R_{out} are the inboard and outboard major radii at the midplane, respectively. We assume $V_\phi \approx V_{||}$, since the poloidal field is small in typical TST-2 LHW sustained plasmas. In addition, we neglect perpendicular velocity V_\perp , because LHW mainly affects $V_{||}$ and then, $V_{||}|_{R_{out}} = V_{||}|_{R_{in}}$. Hereafter, we omit the subscript $||$ from the velocity. Suppose that the LHW increases V by ΔV_{in} at the inboard midplane, then Eq. (1) is rewritten as

$$\begin{aligned} & -eRA_\phi|_{R_{in}} + m_eR_{in}(V + \Delta V_{in}) \\ & = -eRA_\phi|_{R_{out} + \Delta R_{out}} + m_e(R_{out} + \Delta R_{out})(V + \Delta V_{in}). \end{aligned} \quad (2)$$

Here, ΔR_{out} represents the outboard expansion of orbit due to the acceleration ΔV_{in} . The difference between Eqs. (1) and (2) yields

$$\begin{aligned} m_eR_{in}\Delta V_{in} & = -e\frac{\partial RA|_{R_{out}}}{\partial R}\Delta R_{out} \\ & \quad + m_eR_{out}\Delta V_{in} + m_e\Delta R_{out}V \\ & = eR_{out}B_p\Delta R_{out} \\ & \quad + m_eR_{out}\Delta V_{in} + m_e\Delta R_{out}V. \end{aligned} \quad (3)$$

Here, we use Taylor expansion and neglect higher order terms. B_p is the poloidal field strength, and it is calculated from the derivative of poloidal flux as $\partial RA|_{R_{out}}/\partial R = R_{out}B_z = -R_{out}B_p$ ($-B_z = B_p > 0$). Rewriting Eq. (3), we obtain the relationship:

$$\begin{aligned} m_e(R_{in} - R_{out})\Delta V_{in} & = (m_eV + eR_{out}B_p)\Delta R_{out} \\ \Delta R_{out} & = \frac{R_{in} - R_{out}}{V/\Omega_{ep} + R_{out}} \frac{\Delta V_{in}}{\Omega_{ep}} \left(\Omega_{ep} \equiv \frac{eB_p}{m_e} \right). \end{aligned} \quad (4)$$

Here, $\Delta V_{in} < 0$ when the electron is accelerated toward the direction of increasing the plasma current. In this case $\Delta R_{out} > 0$, and the orbit expands outward. This equation indicates that the radial displacement is roughly proportional to the velocity increment, and this is what we call RF induced transport, which is often used to interpret fast ion diffusion in ICRF heating [10]. In a similar manner we obtain the relationship for an outboard acceleration case:

$$\Delta R_{in} = \frac{R_{in} - R_{out}}{-V/\Omega_{ep} + R_{in}} \frac{\Delta V_{out}}{\Omega_{ep}}. \quad (5)$$

These expressions can be further simplified by approximations. In the following simulation, R_{in} and R_{out} are replaced by initial major radii R_{sin} and R_{sout} , respectively, and Ω_{ep} is given as a constant parameter.

A particle model is adopted, and evolutions of many particle orbits, which are expressed by (R_{in}, R_{out}, V) , are calculated based on random walk. The velocity random walk causes particle diffusion in velocity space, and it results in a velocity distribution function. Although the diffusion can be represented by a quasilinear diffusion term of LHW, we adopt a simplified phenomenological diffusion coefficient as a function of velocity. The diffusion coefficient is represented as $\langle \widetilde{\Delta V}^2 \rangle / 2\Delta t$, and the random $\widetilde{\Delta V}$ follows a normal distribution with a given $\langle \widetilde{\Delta V}^2 \rangle$. Δt is the time step in the simulation. Figure 2 shows examples of diffusion coefficients and obtained distribution functions. The distribution function shows a peak at $V = 0$, which represents cold bulk electrons. In our model, $\sqrt{\langle \widetilde{\Delta V}^2 \rangle}$ is a function of V , and it is expressed by an asymmetric Gaussian function:

$$\sqrt{\langle \widetilde{\Delta V}^2 \rangle} = V_{amp} \exp \left[- \left(\frac{V - V_0}{V_{w0} \text{ or } V_{w1}} \right)^2 \right] \times (1 - (V/c)^4). \quad (6)$$

This function shows the maximum at $V_0 \approx c/5$, and it is fixed to the velocity corresponding to 10 keV. This velocity agrees with the designed resonant velocity (with

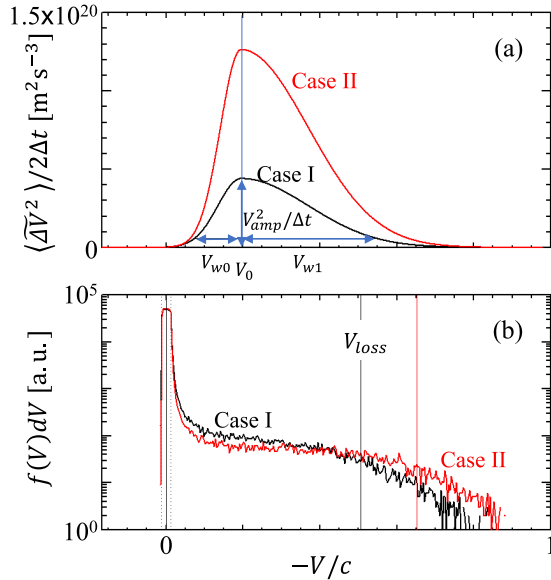


Fig. 2 Diffusion coefficient $\langle \widetilde{\Delta V}^2 \rangle / 2\Delta t$ in parallel velocity space (a) and obtained steady state velocity distribution functions $f(V)dV$ (b). Definitions of V_{amp} , V_0 , V_{w0} , V_{w1} are shown in (a). In these cases $\Delta t = 5 \times 10^{-7}$ s. Two cases: Case I ($R_{sout} = 0.505$ m) and Case II ($R_{sout} = 0.480$ m) are shown, and the difference is described later. The vertical lines in (b) indicate V_{loss} defined by Eq. (7).

$N_{||} = 5$) of the antenna [11]. V_{w0} and V_{w1} are used to express the asymmetric widths. V_{amp} , V_{w0} , V_{w1} are the free parameters defining the diffusion coefficient. The diffusion coefficient has a role to extract electrons from the peak (i.e., bulk components) and drive them to a higher $|V|$. When $|V|$ becomes high the electron tends to reach a limiter and be lost. The representative velocity V_{loss} (< 0) for an electron to reach the outboard limiter is written as

$$|V_{loss}| \equiv \frac{R_{sout} + \frac{V_{loss}}{2\Omega_{ep}} \Omega_{ep} \delta R_{out}}{R_{sout} - R_{sin}} \approx \frac{R_{sout}}{R_{sout} - R_{sin}} \Omega_{ep} \delta R_{out}, \quad (7)$$

where δR_{out} is the distance between the starting point and the outboard limiter (see Fig. 1). The first expression is obtained from Eq. (4) and V_{loss} can be obtained through iteration. Here, the factor of $\frac{1}{2}$ represents the average of V (i.e., average of 0 and V_{loss}). The second expression is more simplified expression, showing that V_{loss} is roughly proportional to $\Omega_{ep} \delta R_{out}$. V_{loss} is the essential parameter determining the confinement of fast electron, and a larger δR_{out} enables confinement of a higher energy electron. This representative velocity is indicated by vertical lines in Fig. 2(b).

Slowing down of fast electron due to the collision with cold electrons, ions and neutrals is another process to affect the distribution functions. While the diffusion effect $\langle \widetilde{\Delta V}^2 \rangle / 2\Delta t$ drives electrons mainly to a higher velocity, the collisions slow the velocity so that the cold bulk component is formed. Figure 3 shows examples of momentum transfer collision frequency as a function of fast electron energy for given densities of cold ion, electron and neutral. The collision frequencies for ion and electron are cal-

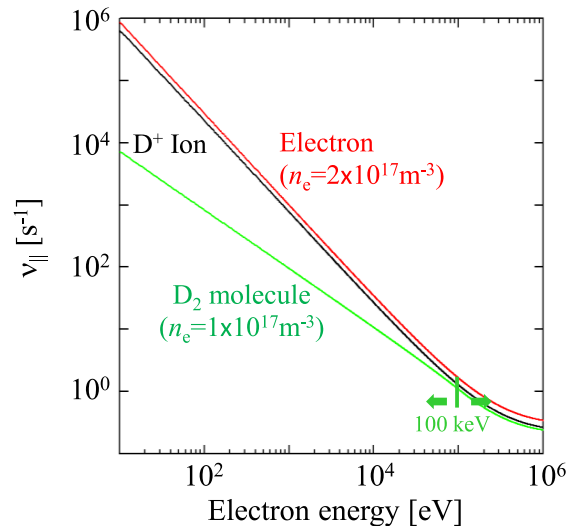


Fig. 3 Momentum transfer collision frequency $\nu_{||}$ as a function of fast electron energy. Here, we use the parameter set: $n_e = 2 \times 10^{17} \text{m}^{-3}$, $Z_{eff} = 1.5$, $n_{D_2} = 1 \times 10^{17} \text{m}^{-3}$, which are the parameters to represent one of typical experimental results in TST-2.

culated from standard Coulomb collisions, but we adopt Coulomb logarithms given in Ref. [12]. For the case of neutral, we extrapolate the data given in Ref. [13] in the range 100 eV - 100 keV by the function:

$$\sigma [\text{m}^2] = 0.14 \times 10^{-20} (E/100 [\text{eV}])^{-1.442}. \quad (8)$$

Above 100 keV, we adopt a standard Coulomb scattering with the molecular radius instead of the Debye length in the calculation of the Coulomb logarithm. The energy of 100 keV was chosen so that the collision frequencies below and above the energy are connected smoothly. The velocity of the target ions, electrons and neutrals are neglected, so that the collision frequency at a low velocity is not accurate, and we skip the slowing down for the electrons of which energy is less than T_e . Thus, the electrons slowing down to the energy below T_e do not suffer from further collisional slowing down, but they diffuse in the energy region $< T_e$ due to the diffusion effect of LHW. As a result, a flat distribution function is formed as shown in Fig. 2(b), and T_e becomes the representative energy of the bulk cold components. Thus, we set T_e be around the measured electron temperature ($T_e \sim 40$ eV). Note that, this skipping of slowing down at low energy is useful to avoid too short time step Δt . Although the slowing down due to neutrals is not significant for typical cases shown in Fig. 3, the neutral density affects the source rate through electron-impact ionization. The rate is calculated from Binary-Encounter-Bethe (BEB) model [14].

In addition to the two velocity variation processes: random walk by LHW and slowing down by collision, acceleration due to macroscopic inductive field E is considered in some cases, and the velocity variation in time step Δt is written as

$$\Delta V = \widetilde{\Delta V} - \nu_{\parallel} V \Delta t - eE/m_e \Delta t, \quad (9)$$

where ν_{\parallel} represents the total collision frequency (i.e., the sum of the three collision frequencies shown in Fig. 3). Here, we omit the differences between the inboard and the outboard acceleration/deceleration to make the explanation easier. The differences are considered later. The velocity variation of a fast electron induces an energy increment $m_e(V + \Delta V)^2/2 - m_e V^2/2$, where m_e includes the relativistic effect. The energy increment can be divided into three terms corresponding to the three terms in the RHS of Eq. (9). The energy increment induced by $\widetilde{\Delta V}$ represents the energy transfer from LHW to fast electrons. This is a random term and the energy transfer can be either positive or negative. When fast electrons are accelerated on average, the fast electrons gain energy and there is a positive power flow from the LHW to the fast electrons. This is what we call the LHW deposition power. The energy increment induced by $-\nu_{\parallel} V \Delta t$ is always negative. The fast electrons lose energy, and the energy is dissipated by cold components, which heat them as a result. When we extract the energy transfer induced by electron-electron collision

($\nu_{\parallel ee}$, red curve in Fig. 3), we can obtain the bulk electron heating power.

In a similar manner, we can distinguish different momentum transfer paths. $\widetilde{\Delta V}$ represents the momentum input from LHW to fast electrons. $|\nu_{\parallel} V \Delta t|$ represents the momentum loss of fast electrons. The total momentum retained by fast electrons is proportional to the driven plasma current. When the distribution function of fast electrons is expressed by $f(V)dV$ (e.g. Fig. 2), the density, toroidal current density and the plasma current are expressed as $n_e = C \int f(V)dV$, $j_{\phi} = C \int f(V)VdV$ and $S j_{\phi}$, respectively. Here, C is a coefficient to convert the calculated electron number to the density, and S is the poloidal cross section of the plasma. In the present study, C is determined so that the plasma current becomes a given value. The momentum transferred from the fast electrons to the bulk electrons can increase the current carried by the bulk electrons. However, the collision between the bulk electrons and ions are frequent due to the low electron temperature ($T_e = 40$ eV in this paper), and the current carried by the cold bulk electrons is negligible. By adding the effects of fast electron loss at a limiter, we can consider the energy flow, momentum flow and particle flow via fast electrons. In the case of particle flow, however, we need to consider particle flows of bulk components, which we assume to be proportional to the particle flow of fast electrons.

The differences between the inboard and the outboard velocity variation should be considered to express the RF induced transport, and Eq. (9) is rewritten as

$$\begin{aligned} \Delta V_{in} &= \gamma_{RF} \widetilde{\Delta V} - \gamma_c \nu_{\parallel} V \Delta t - \gamma_E eE/m_e \Delta t, \\ \Delta V_{out} &= (1 - \gamma_{RF}) \widetilde{\Delta V} - (1 - \gamma_c) \nu_{\parallel} V \Delta t \\ &\quad - (1 - \gamma_E) eE/m_e \Delta t, \end{aligned} \quad (10)$$

where ν_{\parallel} represents the total collision frequency, and Gammas (γ_{RF} , γ_c , γ_E) represent the ratio of the inboard and the outboard contributions to the velocity variation. Here, we use different $\widetilde{\Delta V}$ s in the two lines in Eq. (10) to avoid correlation between the inboard and the outboard velocity changes. It is reasonable to assume that LHW induced velocity increment ($\widetilde{\Delta V}$) mainly occurs at the inboard peripheral region (i.e., $\gamma_{RF} \sim 1$), because of the following theoretical and experimental results. The LHW power is expected to be deposited mainly at the inboard peripheral regions due to the toroidal effect and due to the poloidal field effect in a spherical tokamak configuration [7, 8], and the bulk electron temperature profile is hollow [15], and an equilibrium reconstruction suggests a hollow current density profile [16]. γ_c is the ratio for collisions and this should be proportional to the staying time at the inboard side. The staying time is proportional to the field line length when the perpendicular velocity is negligible. The representative ratio of the inboard field line length to the outboard field line length is about 4 due to the low aspect ratio configuration. In this case, γ_c becomes 0.8. For the case of γ_E , we should also consider $1/R$ effect in the relationship

between the loop voltage and the toroidal field E when a loop voltage is given. As a result, γ_{RF} , γ_c , γ_E cannot be determined accurately, and we consider them as adjustable free parameters in the range $1/2 < \gamma_{RF}, \gamma_c, \gamma_E < 1$.

The orbit (R_{in}, R_{out}, V, t) of many electrons (typically 0.1 - 1 million electrons) are calculated for given parameters: initial positions (R_{sin}, R_{sout}) with random spread represented by ΔR_s , parameters to define the LHW effect $(V_{amp}, V_{w0}, V_{w1})$, poloidal field strength B_p , neutral molecule density n_{D_2} , gammas γ_{RF} , γ_c , γ_E , electron temperature $T_e = 40$ eV and a fuelling efficiency $\eta = 0.2$. The parameter η describes the ratio of fast electron loss at the limiter to the loss of bulk electrons (through either anomalous transport or neoclassical transport). We calculate the former in our model, while we speculate the latter by multiplying the former by $1/\eta$. At a steady state, the lost electrons should be supplied through electron impact ionization of neutral molecule, and we can determine n_{D_2} so that a steady state is obtained. In practice, the introduction of $\eta (< 1)$ enhances the speculated n_{D_2} by about $1/\eta$. It should be noted that the (bulk) particle confinement time becomes η -times of the fast electron confinement time. When an electron reaches either the outboard limiter (at $R = 0.585$ m) or the inboard limiter (at $R = 0.13$ m), we reset the orbit and start a new orbit from $(R_{sin} + \Delta R_s, R_{sout} + \Delta R_s, V = 0, t)$.

As the calculation proceeds a near steady state is obtained and then the free parameters $(V_{amp}, V_{w0}, n_{D_2})$ are adjusted to reproduce the measured parameters of the target plasmas: electron density $n_e = 2 \times 10^{17} \text{ m}^{-3}$, and RF power $P_{RF} = 60$ kW. Here, the electron density is calculated from the average current density $en_e \langle V \rangle = j_{av} = I_p/S$ where $I_p = 18$ kA is the plasma current and S is the poloidal cross section. After a sufficient time, we obtain a steady state electron velocity distribution function, and energy distribution of the lost electrons per unit time. The latter is used to calculate thick target X-ray emission. In addition, we can obtain power transfer from LHW to fast electrons by summing up the energy variation in each random walk (ΔV) , and this power corresponds to LHW (deposition) power $P_{RF} (= 60$ kW). Similarly, we obtain power transfer from fast electrons to bulk electrons from $\nu_{||ee} V \Delta t$, where $\nu_{||ee}$ is the fast electron-bulk electron collision frequency. This corresponds to bulk electron heating power. We also obtain particle loss rate, which leads to a particle confinement time.

3. X-Ray Emission Model

An X-ray emission model is constructed to predict the measured hard X-ray spectrum for the steady state fast electrons. The X-ray emission model based on several simplifications and factors of uncertainty could be induced. One additional uncertainty arises from the fact we have not yet identified the exact fast electron hitting points, which are probably located on a limiter among the five molyb-

denum limiters in TST-2. Therefore, we placed an LYSO scintillator far ($R = 3.3$ m) from the TST-2 device to measure the average hard X-ray flux from the device, and made a 0-dimensional model to predict the flux. Figure 4 shows the schematic top view of the TST-2 device, in which the assumed processes between the fast electron loss and the X-ray detection are illustrated.

The four elementary processes are shown in Fig. 5. The first process is the thick target X-ray generation in a molybdenum limiter by a fast electron (Fig. 5(a)). We use the method described in Ref. [17], which is developed to explain the absolute X-ray spectrum generated by an X-ray tube. The spectrum is a function of incident angle and energy of a fast electron, and X-ray emitting angle. We assume normal incidence and sum up over different backward emitting angle θ . Here, the calculated forward emission is much smaller than the backward emission for the molybdenum limiter thickness of 5 mm. Since the candidate limiter surface is located on the opposite side with respect to the detector location side (see Fig. 4), we assume that a thick target X-ray should be reflected once at the stainless steel vacuum vessel wall (with a thickness of 7 mm) toward the plasma side (Fig. 5(b)) and should penetrate through the vacuum vessel wall once (Fig. 5(c)) to reach the scintillator. The process (a) and (b) depends on the incident angle and emitted angle θ . In order to include various angles with a relatively simplified calculation method, we assume normal incidence for (a) and (b),

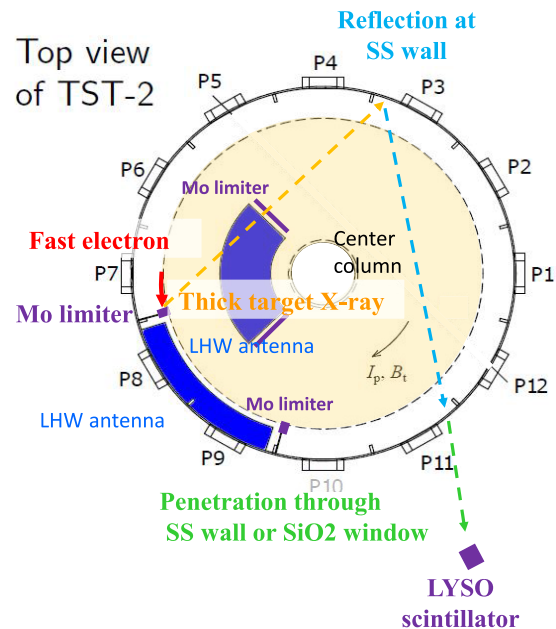


Fig. 4 Schematic top view of the TST-2 device. The assumed x-ray detection processes (incidence of a fast electron on a molybdenum limiter, thick target X-ray generation at the limiter, reflection of the X-ray at the wall, penetration of the X-ray through the wall, and detection of the X-ray by a scintillator) are also illustrated.

while for emitted angle θ we calculate the integration over the hemisphere: $\int_0^\pi 2\pi \sin(\pi - \theta)d\theta \times$.

The reflection process (Fig. 5(b)) is divided into three steps; (i) a thick target X-ray hits the wall with normal angle and penetrate through a certain distance, (ii) and it is back scattered once, (iii) and it penetrates through the wall again to be emitted from the wall. Note that the penetration efficiency is mainly affected by photon absorption, and the efficiency can be calculated from the attenuation coefficient μ . We sum up the absorption coefficients of the forward and backward penetration processes to calculate the probability of the penetrations. The backward scattering consists of Rayleigh scattering (i.e., elastic scattering) and Compton scattering.

Considering different penetration distance (by integrating along the distance) the reflectivity due to the Rayleigh scattering is given as

$$n_A \frac{d\sigma_R}{d\Omega} \frac{2\pi \sin(\pi - \theta)d\theta}{\mu_0(1 + 1/\cos(\pi - \theta))}, \quad (11)$$

where n_A is the atom number density, $\frac{d\sigma_R}{d\Omega}$ is the differential cross section of Rayleigh scattering calculated from the atomic form factor of iron [18]. Here, we use iron instead of the mixture of iron, chromium and nickel, because they have similar Z s. μ_0 is the attenuation coefficient in stainless steel for the incident X-ray energy. This reflectivity is a function of incident X-ray energy and backward reflection angle $\pi - \theta$, and the energy of the reflected X-ray is the same as that of incident X-ray. When the X-ray energy is high, it would pass through the vacuum vessel (of thickness 7 mm) without scattering, but it can be scattered by the structures outside the vacuum vessel, and it may penetrate through the vessel again. In fact, X-rays scattered by objects around the device are non-negligible in the measurements. Such scattering effects can be simulated by increasing the vacuum vessel thickness. Thus, we assume that the thickness of the wall is infinite in deriving the expression (11). This assumption makes the expression simple, and a similar assumption is made for the case of Compton scattering. Note that the difference between the finite range (i.e., 0 - 7 mm) and infinite range integrations is small and it is less than 2% at $E = 100$ keV, $\theta = 0$.

The reflectivity due to Compton scattering can be written by

$$n_A \frac{d\sigma_C}{d\Omega} \frac{2\pi \sin(\pi - \theta)d\theta}{\mu_0 + \mu(E(\pi - \theta)) / \cos(\pi - \theta)}, \quad (12)$$

where $E(\pi - \theta)$ is the energy of the scattered X-ray, and the energy depends on the scattering angle. $\mu(E)$ is the corresponding attenuation coefficient. In the third process the reflected X-ray has to penetrate through the vacuum vessel (Fig. 5(c)). Here, we assume the incident angle is 45 degrees. Since a part of the vacuum vessel has a quartz window, we include the contribution of the window in the calculation of penetration probability. When an X-ray reaches the LYSO scintillator with a height of 1 inch, almost all

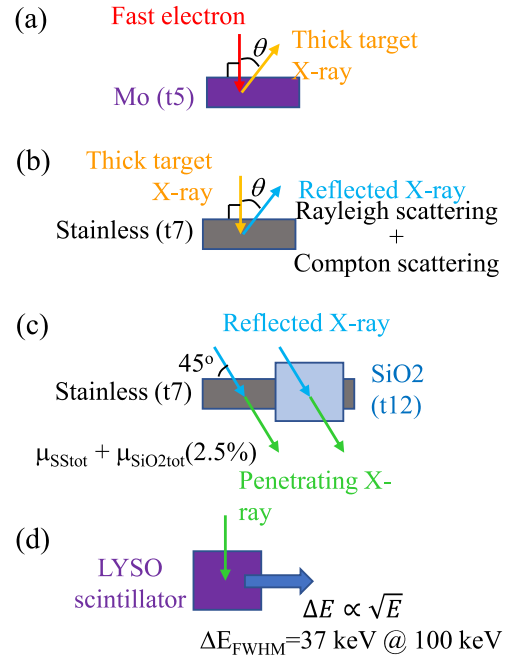


Fig. 5 Four processes between a fast electron incidence and an X-ray signal detection. Thick target X-ray generation (a), reflection of X-ray by the vacuum vessel wall (b), penetration through the vacuum vessel wall (c) and detection of X-ray by a scintillator (d).

X-rays are detected, but the obtained energy has a finite spread due to the finite number of scintillation photons, and the effect is calculated by the convolution of the energy resolution. From these processes we predict the energy spectrum of the detector for a given energy distribution function of the fast electrons hitting a limiter. Thus, we can compare it and the measured hard X-ray spectrum.

4. Calculation Results and Comparison with Experiments

Firstly, results of a case, where the model parameters are chosen to reproduce a discharge, is shown. Some obtained quantities, such as bulk electron heating power and particle confinement time are discussed. Secondly, calculated and measured X-ray spectra for two discharges are shown to see the qualitative agreement of the spectral shape.

Figure 6(a) is the energy distribution of fast electrons at two different times. Here, the time indicates the time from the start of the calculation, where electrons are cold. The velocity space diffusion representing the LHW effect tends to accelerate the cold electron, and the electron energy distribution spreads. In the first phase, the electron density tends to be high, because the plasma current I_p is fixed to the target I_p and the density n_e (i.e., weight of each electron) is recalculated to achieve the target I_p . After a certain time (6 ms in the case of Fig. 6), n_e and the

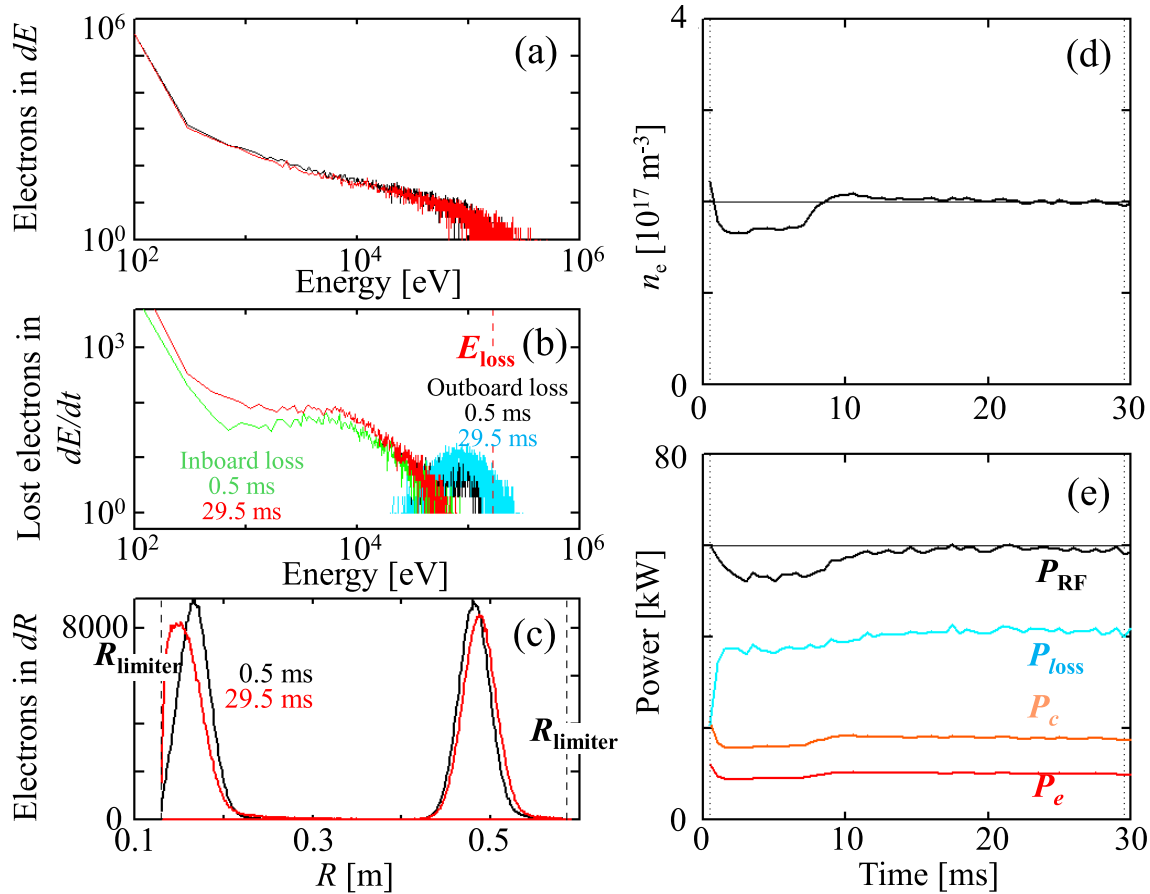


Fig. 6 Calculation results. Energy distribution of the electrons (a), energy distributions of lost electrons (b), radial profiles (i.e., R_{in} and R_{out} distributions) of electrons (c), time evolutions of electron density (d) and powers (e) are shown. Different colors in (a) - (c) represents distributions at different times. Dashed lines in (c) represent the limiter positions. P_{RF} , P_{loss} , P_c and P_e in (e) denote the LHW deposition power, electron loss power at the limiters, collisional loss power and bulk electron heating power, respectively.

LHW deposition power P_{RF} are adjusted to reproduce the target n_e and P_{RF} by changing the model parameters V_{w0} , V_{amp} . The converging process of n_e and P_{RF} can be seen in Figs. 6(d) and (e). Figure 6(b) shows the energy distributions of the lost electrons, which hit either the outboard or the inboard limiter. The vertical line indicates the energy E_{loss} corresponding to the representative lost electron velocity defined by Eq. (7). In the cases we obtained so far, the energy of the electrons hitting the inboard limiter is lower than that of the electrons hitting the outboard limiter. This is due to the fact that electrons must experience both (inboard) acceleration and (outboard) deceleration to hit the inboard limiter as shown by the red orbit in Fig. 1, while they do not have to experience deceleration to hit the outboard limiter. Examples of the outboard lost and the inboard lost orbits will be shown in Sec. 5.

Figure 6(c) shows the radial distributions (R_{in} and R_{out}) at two times. The number of electrons is constant in the model, and the lost electrons are supplied at R_{sin} ($= 0.17$ m) and R_{sout} ($= 0.48$ m). The electrons diffuse from these initial positions and they are lost when they reach either the outboard or the inboard limiter. The power flow

can be seen in Fig. 6(e). The deposited LHW power is $P_{RF} \approx 60$ kW, which is an experimental value of a discharge we want to reproduce. About 40 kW ($= P_{loss}$) is lost by fast electrons hitting a limiter, and the residual power of about 20 kW ($= P_c$) are lost by collisions, which results in the heating of cold electrons, ions and neutrals. It should be noted that the energy transfer is not explicitly considered in the calculation, but we only consider the parallel velocity of fast electrons, and the perpendicular velocity is assumed to be zero. Thus, the decrease in the fast electron energy should be transferred to cold electrons, ions and neutrals.

Among the 20 kW, about 10 kW ($= P_e$) is used to heat bulk electrons. Using the bulk electron heating power and an appropriate energy confinement time, we can estimate the bulk electron temperature and compare it with the typical experimental temperature of 40 eV. Here we use ITER L-mode scaling law [19], then the energy confinement time becomes about 0.6 ms, and the temperature becomes 120 eV. If we adopt the LHW power of 60 kW in the formula, then the energy confinement time becomes 0.16 ms and the bulk electron temperature becomes 50 eV

(for the heating power of 10 kW). Calculations with ITER 89-P, -IPB98(y,2) yield different temperatures within a factor less than ten. Thus, we can conclude that these standard energy confinement times are consistent with the estimated bulk electron heating power of 10 kW within a factor of ten. In other words, the bulk electrons can be heated by collisions with fast electrons. It should be noted that not only the bulk electron heating but also the ion heating is expected and this is probably the reason we observe an impurity ion temperature of around 10 eV [20].

The particle confinement time calculated from the fast electron loss rate is about 5 ms for the case of Fig. 6. Since we set $\eta = 0.2$, the bulk electron source is 4 times larger than the fast electron loss rate, and then the particle confinement time for bulk electrons becomes about 1 ms. This is longer than or similar to the energy confinement times shown above. The source is provided by the electron impact ionization of neutral gas with the estimated density of $n_{D_2} \sim 1 \times 10^{17} \text{ m}^{-3}$, which is about an order of magnitude smaller than the experimental initial filling pressure. Usually, the pressure inside the vacuum vessel decreases quickly during a discharge due to wall pumping [21], and penetration depth of neutrals is very long in the present low density plasmas. Thus, the estimated n_{D_2} seems to be reasonable. It should be noted that when we set $\eta = 1$, then n_{D_2} becomes about $2 \times 10^{16} \text{ m}^{-3}$, and particle confinement time for bulk electrons becomes infinite.

Figure 7 shows hard X-ray spectra from two similar discharges with almost the same plasma current of $I_p = 18 \text{ kA}$ and the LHW injection power of $P_{RF} \approx 60 \text{ kW}$. The major difference between them is the outboard LCFS

position $R_{LCFS} = 0.515, 0.54 \text{ m}$ (see Fig. 1 for the definition of R_{LCFS}). The difference in R_{LCFS} would cause a difference in R_{sout} . Therefore, we can expect a larger δR_{out} for a smaller R_{LCFS} , and we can also expect confinement of a higher energy electron for a smaller R_{LCFS} (see Eq. (7)). In the calculations, we adjust the parameters: V_{amp} , V_{u0} , n_{D_2} for each case to reproduce experimental parameters: $n_e = 2 \times 10^{17} \text{ m}^{-3}$, $P_{RF} = 60 \text{ kW}$ (and $I_p = 18 \text{ kA}$). The other major common parameters are as follows. $B_p = 0.008 \text{ T}$, $\gamma_{RF} = 0.8$, $\gamma_c = 0.75$, $T_e = 40 \text{ eV}$, $\eta = 0.2$, $R_{sin} = 0.17 \text{ m}$. The difference between the two discharges with $R_{LCFS} = 0.515, 0.54 \text{ m}$ are simulated by the difference in the outboard starting point $R_{sout} = 0.480, 0.505 \text{ m}$, respectively. Here, R_{sout} s are chosen so that $R_{LCFS} - R_{sout}$ are the same for the two cases. The other common parameters are adjusted to reproduce the hard X-ray spectrum as well as possible, paying attention that the parameters are reasonable. The spectral shape and difference between the two discharges are qualitatively well reproduced. Although the calculated absolute fluxes are several times larger than the experimental ones, such differences could easily happen due to the simplifications in the X-ray emission models. It should be noted that when we assume that the thick-target X-ray can directly reach the detector without the wall reflection process (Fig. 5(b)), the flux becomes about 10^2 times large. When we adopt standard bremsstrahlung in plasma, then the flux becomes about 10^3 times small. These estimations indicate that the present four processes in the X-ray emission model are reasonable.

5. Discussion

Firstly, we show some trajectories of lost electron to explain the different behaviours of the outboard loss and the inboard loss processes. Secondly, we estimate the perpendicular velocities, and show they are negligible. Thirdly, we discuss the role and impact of the present model comparing with more sophisticated conventional codes.

Figure 8(a) shows $E_{||}(t)$ from the start to the end (i.e., born-lost). When the energy is low, collisional slowing down is significant and the electron tends to stay at the low energy region, but once the energy becomes high, the high diffusivity (see Fig. 2(a)) and the low collisionality cause quick diffusion and quick loss at the limiter. The shape of the resultant velocity distribution function (e.g. Fig. 2(b)) reflects such competing processes. Since most of the electrons are moving in the current carrying direction ($V < 0$), the velocity acceleration ($\Delta V < 0$, $|\Delta V| > 0$) causes increases in R_{in} and R_{out} (see Eqs. (4), (5)) and energy increases as shown in Figs. 8(a) and 8(b). In the present situation, the energy increase and resultant outboard limiter loss is the dominant power loss process. For the inboard loss, velocity deceleration ($\Delta V > 0$) and resultant energy decrease is necessary. As a result, the energy at the time

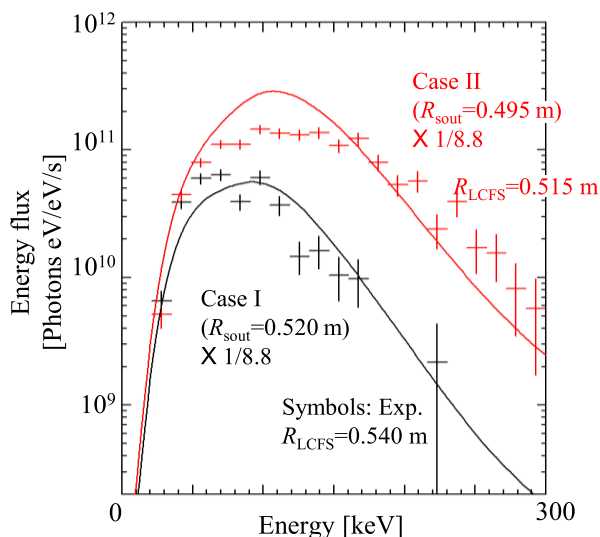


Fig. 7 Calculated (solid curve) and measured (plus symbols) energy spectra detected by a scintillator. The calculated spectra are obtained by using the energy distribution of lost electrons in the model. They are multiplied by a factor of 1/8.8 in the plot. The corresponding distribution functions are shown in Fig. 2(b).

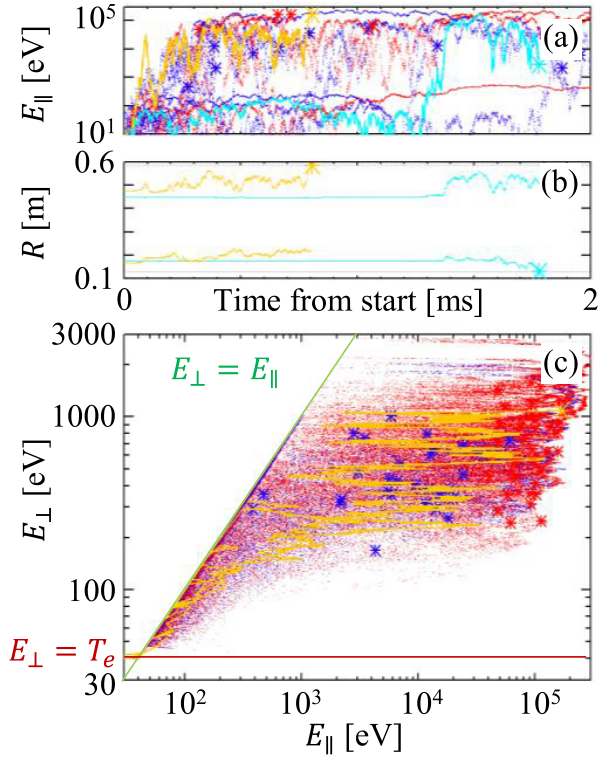


Fig. 8 Trajectories of fast electrons. $E_{\parallel}(t)$ s of 20 electrons from the start to the end (i.e., born-lost) (a), R_{out} and R_{in} of 2 electrons (b) and 71 trajectories in $E_{\parallel} - E_{\perp}$ plane (c) are shown. The red dots and orange curves represent the outboard lost electrons and the blue dots and light blue curves represent the inboard lost electrons. Asterisks denote the end point. The green line in (c) represents $E_{\parallel} = E_{\perp}$, below which E_{\perp} is forced to be.

reaching the inboard limiter tends to be low as shown by blue asterisks in Figs. 8(a) and 8(c).

Perpendicular velocities (V_{\perp} s) were neglected in deriving Eq. (1) without quantitative evaluation, but now we can estimate the collisional increase in V_{\perp} using the obtained time evolutions of V_{\parallel} . V_{\parallel} s are accelerated on average by LHW, and slowed down through collisions with a total collision frequency of ν_{\parallel} . Simultaneously, the collision causes diffusion or increase in V_{\perp} . The equation for the perpendicular energy E_{\perp} is written as [22]

$$\frac{dE_{\perp}}{dt} = \nu_{\perp} E. \quad (13)$$

Here, ν_{\perp} is the perpendicular diffusion frequency and the value is $\nu_{\perp} = (1-2) \times \nu_{\parallel}$. The range 1-2 represents the effect of mass ratio. Hereafter, we adopt $\nu_{\perp} \equiv 2\nu_{\parallel}$. The above equation indicates that E_{\perp} (and V_{\perp}) increases gradually and $E_{\perp}(t)$ depends on E and $\nu_{\perp}(E) = 2\nu_{\parallel}(E)$. Therefore, we can expect that when the acceleration is sufficiently fast, there would be no time for E_{\perp} to grow. Here, we assume such a situation and use E_{\parallel} and $\nu_{\parallel}(E_{\parallel})$, instead of E and $\nu_{\parallel}(E)$. Then we can obtain $E_{\perp}(t)$ for a given $E_{\parallel}(t)$.

In order to estimate the typical E_{\perp} , we performed a

numerical calculation using $E_{\parallel}(t)$ (and $\nu_{\parallel}(E_{\parallel})$) obtained by the RF induced transport model. The actual calculation process is as follows. Since the bulk cold electron temperature is $T_e (= 40 \text{ eV})$, the initial condition is set to be $E_{\perp}(0) = T_e$. Using the difference equation with time step Δt , i -th $E_{\perp}(t_i)$ is calculated by

$$\hat{E}_{\perp}(t_i) = E_{\perp}(t_{i-1}) + 2\nu_{\parallel} E_{\parallel}(t_i) \Delta t, \quad (14)$$

where $\hat{E}_{\perp}(t_i)$ is a tentative perpendicular energy. Two modifications should be made on this process. Firstly, $E_{\perp} \geq T_e$, because we assume bulk electrons with a temperature T_e . Secondly, $E_{\perp} \leq E_{\parallel}$, because $E_{\perp} \sim E_{\parallel}$ is the relaxed isotropic situation, further diffusion in E_{\perp} tends to be suppressed. Then i -th $E_{\perp}(t_i)$ is given by

$$E_{\perp}(t_i) = \text{Max}[T_e, \text{Min}[\hat{E}_{\perp}(t_i), E_{\parallel}(t_i)]]. \quad (15)$$

Figure 8(c) shows the results for 71 electrons. The increase in E_{\perp} is fast in low energy regions and slow at high energy regions. As a result, the maximum E_{\perp} is less than 3 keV in this case. The average perpendicular energies for the electrons with $E_{\parallel} > 1 \text{ keV}$ and $E_{\parallel} > 10 \text{ keV}$ are 790 eV and 860 eV, respectively. E_{\parallel} s and resultant orbit deviations can be modified by the ratio of about E_{\perp}/E_{\parallel} , and the transport is modified by a similar ratio. The typical energy of lost electrons is 100 keV, and then $E_{\perp}/E_{\parallel} \sim 10^{-2}$. Thus, the effects on the transport and the loss are negligible.

The present model is a simplified model, and many physics were neglected. We have often used the combination of GENRAY (a ray tracing chord) and CQL3D (a Fokker-Planck solver) as a conventional tool to understand the LHW sustained plasmas [8]. The calculation was performed iteratively, and the electron distribution function is obtained self consistently. Although some experimental behaviors were explained by the conventional tool, the value of driven current was about an order of magnitude higher than the experimental current [8]. Thus, the conventional tool is not perfect, and we need additional physics to explain the low experimental current. The present model takes into account inboard-outboard asymmetric orbit expansion, and the present results suggest such orbit expansion is the dominant loss mechanism of fast electrons. That is the RF induced transport. In contrast, CQL3D adopts bounce averaged Fokker-Planck equations on a flux surface, and such orbit expansion cannot be taken into account explicitly. In addition to the RF induced transport, thick-target X-ray emission is calculated in our model. This is quite important in the low density plasma (e.g. $\sim 10^{17} \text{ m}^{-3}$) because the Bremsstrahlung in plasma are expected to be $10^{-2} - 10^{-4}$ of those in standard plasmas, while the thick-target X-ray is larger than those due to the RF induced transport. Note that CQL3D is developing, and the present work would contribute to the development of the code.

According to the results of the present model, a moderate density increment and the outboard LHW power deposition are preferable. The former would enhance the

slowing down of fast electrons, and the latter would invoke orbit shrink toward the magnetic axis (i.e., outward movement of R_{in}). Both are useful to reduce the RF induced transport. The plasma current, however, is affected not only by the transport (i.e., loss), but also by the number of fast electrons. According to some preliminary calculations, the transport decreases with the increase in density, but the number of fast electrons decrease due to the enhanced slowing down. As a result, the plasma current change becomes small. Further calculations and analyses are needed to find the condition increasing the driven plasma current. Obviously, wave physics should be considered to make such an increase. A new approach or a new antenna design considering these new effects is necessary for further increase in driven current.

6. Conclusions

An electron transport model is constructed to simulate fast electrons in TST-2 LHW sustained plasmas. Electron generation, electron acceleration by LHW and deceleration by collisions, and electron loss at the limiters are considered. An X-ray emission model is constructed to simulate X-ray emissions, in which thick-target X-ray generation by the fast electrons hitting a limiter is included. The measured X-ray spectra for two discharges with different distances between the LCFS and the outboard limiter are qualitatively reproduced. According to the model, a major part of the LHW deposition power is lost by fast electrons hitting the outboard limiter, while a minor part is used to heat cold bulk electrons. The estimated bulk electron heating power is consistent with the measured typical electron temperature when we adopt an appropriate energy confinement time. Furthermore, the estimated particle confinement time and neutral density are reasonable. Thus, the model can interpret the major features of the fast electrons in LHW sustained TST-2 plasmas. The present work suggests that the RF induced transport of fast electrons is the

dominant loss mechanism.

Acknowledgments

This work is supported by National Institute for Fusion Science Collaboration Research Programs NIFS18KOAR022 and NIFS20KUTR155. This work is also supported in part by Japan/US Cooperation in Fusion Research and Development and US DoE Cooperative Agreement DE-FC02-04ER54698.

- [1] Y. Takase *et al.*, Nucl. Fusion **41**, 1543 (2001).
- [2] Y. Takase *et al.*, Nucl. Fusion **51**, 063017 (2011).
- [3] Y. Takase *et al.*, Nucl. Fusion **53**, 063006 (2013).
- [4] T. Wakatsuki *et al.*, Nucl. Fusion **54**, 093014 (2014).
- [5] T. Shinya *et al.*, Nucl. Fusion **55**, 073003 (2015).
- [6] T. Shinya *et al.*, Nucl. Fusion **57**, 036006 (2017).
- [7] S. Yajima *et al.*, Plasma Fusion Res. **13**, 3402114 (2018).
- [8] N. Tsujii *et al.*, Nucl. Fusion **57**, 126032 (2017).
- [9] A. Ejiri *et al.*, 27th Int. Conf. Fusion Energy 2018 IAEA-CN-258 (Proc. 27th Int. Conf. Fusion Energy 2018, Gandhinagar (Ahmedabad) Gujarat, India, 2018) IAEA, Vienna (2018).
- [10] L. Chen *et al.*, Nucl. Fusion **28**, 389 (1988).
- [11] S. Yajima *et al.*, Nucl. Fusion **59**, 066004 (2019).
- [12] M. Honda, Jpn. J. Appl. Phys. **52**, 108002 (2013).
- [13] A. Hayashi, internal report Inst. Plasma Phys. (IPPI. AM-19) Nagoya Univ., Japan (1981).
- [14] Y.K. Kim *et al.*, it NIST: Electron-Impact Cross Section Database - Intro <https://physics.nist.gov/PhysRefData/Ionization/intro.html>
- [15] H. Togashi *et al.*, Plasma Fusion Res. **10**, 1202082 (2015).
- [16] N. Tsujii *et al.*, Plasma Fusion Res. **15**, 2402010 (2020).
- [17] D.M. Tucker *et al.*, Medical Physics **18**, 211 (1991).
- [18] Atomic form factors, <http://lampx.tugraz.at/~hadley/ss1/crystaldiffraction/atomicformfactors/formfactors.php>
- [19] S.M. Kaye *et al.*, Nucl. Fusion **37**, 16657 (1997).
- [20] S. Tsuda *et al.*, Plasma Fusion Res. **10**, 1202064 (2015).
- [21] T. Yoshinaga *et al.*, J. Plasma Fusion Res. **81**, 333 (2005).
- [22] J. Wesson *Tokamaks 4th ed.* (Oxford Univ. Press, 2011).